Contents lists available at SciOpen

Food Science and Human Wellness

journal homepage: https://www.sciopen.com/journal/2097-0765

China Food Publishing Co.

Investigation of the efficacy of sunflower receptacle flavonoids in treating hyperuricemia: an integrated approach

Kaiyu Wang[1], Kaifeng Liu[1], Huizi Cui[1], Xueqi Fu, Wannan Li*, Weiwei Han*

Key Laboratory for Molecular Enzymology and Engineering of Ministry of Education, Edmond H. Fischer Signal Transduction Laboratory, School of Life Sciences, Jilin University, Changchun 130012, China

ARTICLE INFO

Article history:
Received 14 July 2024
Received in revised form 14 August 2024
Accepted 20 September 2024

Keywords:
Sunflower receptacle flavonoids
Hyperuricemia
Liquid chromatography-mass spectrometry
Gaussian accelerated molecular dynamics simulation
Markov state model

ABSTRACT

Sunflower, a key agricultural crop with a history of use in Chinese medicine, holds potential for hyperuricemia treatment. This study investigates the efficacy and mechanisms of flavonoids extracted from sunflower receptacles in managing hyperuricemia. Various ethanol extracts were tested in hyperuricemia rats to evaluate their effects on uric acid reduction, joint swelling alleviation, and liver and kidney damage. The 30% ethanol extract showed the most significant effects, reducing uric acid levels, alleviating joint swelling, and minimizing liver and kidney damage. Liquid chromatography-mass spectrometry analysis identified 16 active flavonoid compounds in this extract. Molecular docking and machine learning analysis identified quercetin as the strongest xanthine oxidase (XO) inhibitor, with apigenin 7-glucoside emerging as a novel candidate. Further computational studies, including Gaussian accelerated molecular dynamics simulations, energy landscape analysis, and Markov state models, revealed a similar XO inhibition mechanism to allopurinol for quercetin. Our findings underscore the therapeutic potential of sunflower receptacle flavonoids for hyperuricemia management. This research paves the way for incorporating sunflower-derived flavonoids into modern pharmacological approaches for hyperuricemia treatment.

1. Introduction

Hyperuricemia, a metabolic disorder marked by rising incidence and prevalence among younger populations, increasingly draws global concern due to its capacity to cause serious health complications, including gout and uric acid nephropathy[1-3]. Current pharmacological strategies, primarily focus on reducing uric acid synthesis or promoting its excretion, often employ drugs like allopurinol, benzbromarone, and febuxostat[4-6]. However, these medications are frequently linked to severe side effects such as vomiting, nausea, and abdominal pain[7-8]. Xanthine dehydrogenase (XDH), under specific pathological conditions, can convert into xanthine oxidase (XO). Both of these enzymes play pivotal roles in the conversion of hypoxanthine and xanthine into uric acid. These enzymes termed xanthine oxidoreductase (XOR), and they represent a critical target in regulating uric acid levels[9-11].

Sunflower (*Helianthus annuus* L.), a native of South America introduced to China in the 17th century, is widely cultivated in Northeast China[12]. Its receptacles, rich in medicinal properties and particularly effective in gout treatment, contain high levels of flavonoids known for their anti-tumor, antibacterial activities, and capabilities in reducing blood pressure and glucose levels[13-14]. Studies on ethanol extracts from sunflower receptacles have demonstrated their potential in lowering serum uric acid levels and ameliorating symptoms of gouty arthritis in rat models[15]. Yet, the specific bioactive components and their mechanisms of action remain unidentified, posing significant challenges for production and safety in clinical applications[16].

In this context, computational chemistry emerges as a powerful tool in drug design, offering cost-effective virtual screening techniques to facilitate drug discovery[17]. Previous research has variably employed molecular dynamics (MD) and machine learning to explore allosteric inhibitors of XO, revealing critical insights into enzyme dynamics

[1] These authors contributed equally to this work.

* Corresponding authors at: School of Life Sciences, Jilin University, Changchun 130012, China.
E-mail address: liwannan@jlu.edu.cn (W.N. Li); weiweihan@jlu.edu.cn (W.W. Han).

Peer review under responsibility of Beijing Academy of Food Sciences.

SciOpen Publishing services by Tsinghua University Press

http://doi.org/10.26599/FSHW.2024.9250408

and inhibitor efficacy[17-19]. This study explores the therapeutic potential of sunflower receptacle flavonoids against hyperuricemia through comprehensive analysis. The impact of various concentrations of sunflower receptacle ethanol extracts was assessed in rat models. A 30% ethanol extract was found to substantially reduce uric acid levels, alleviate joint swelling, and mitigate liver and kidney damage. Through liquid chromatography-mass spectrometry (LC-MS) analysis, 16 active flavonoid molecules were identified, with quercetin standing out as a particularly effective XO inhibitor and apigenin 7-glucoside as a novel XO inhibitor. Further, Gaussian accelerated MD simulations, energy landscape analysis, and Markov state models (MSM) suggested that the inhibitory mechanism of quercetin is akin to that of allopurinol. These findings underscore the potential of sunflower receptacle flavonoids in managing hyperuricemia and pave the way for the sustainable development of plant-based therapeutic agents. The work flow of our study is shown in Fig. 1.

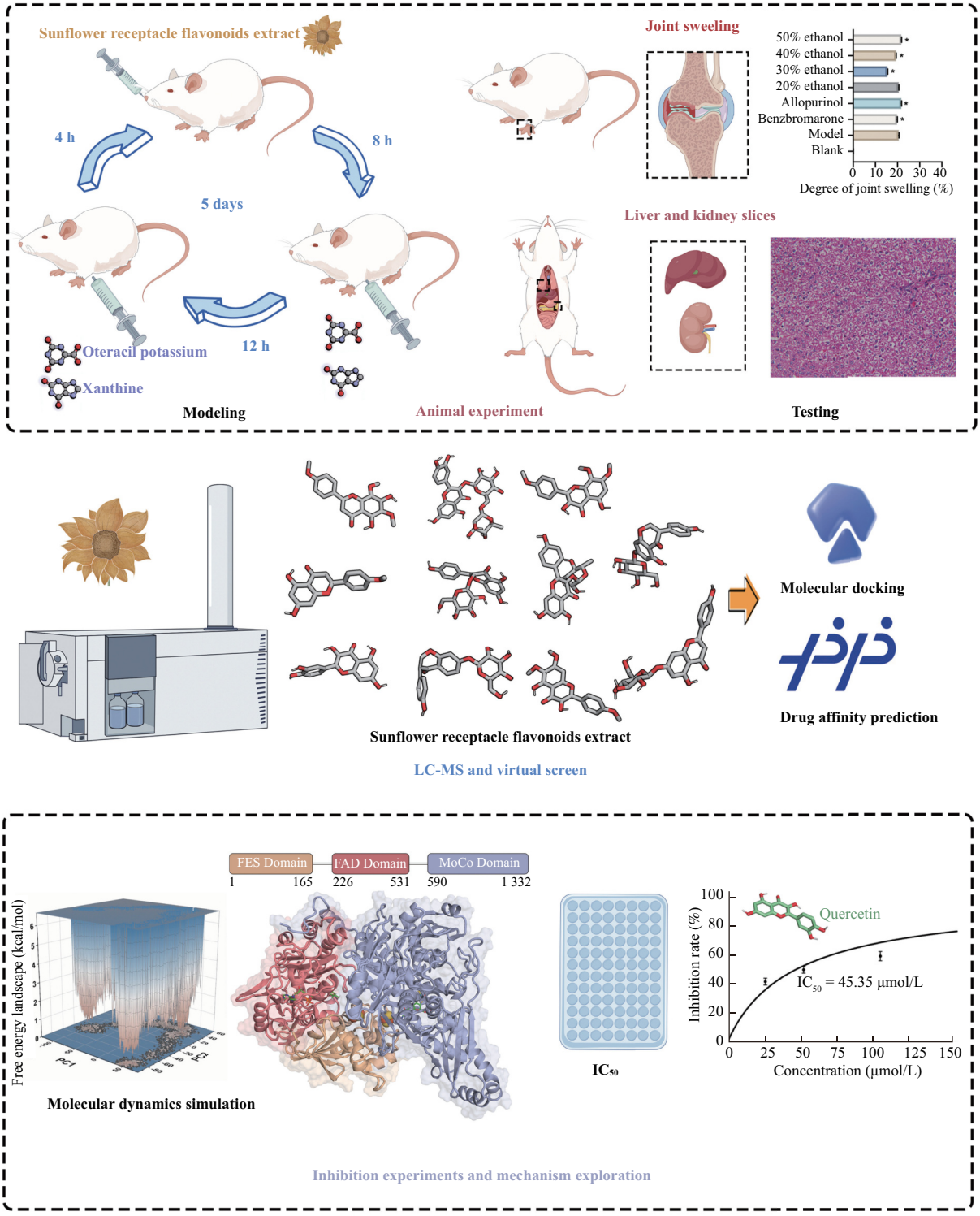

Fig. 1 Work flow of this study.

2. Materials and methods

2.1 Materials

Sunflower receptacles medicinal material, supplied by Jilin Special Medical Food Co., Ltd. (China), was ground before use. Methanol and acetonitrile (chromatographic grade, Fisher, USA), formic acid (chromatographic grade, ROE, USA), 95% ethanol (analytical grade, Beijing Chemical Plant, China), ultrapure water (18.2 MΩ·cm), sodium formate, and leucine enkephalin (Milford, USA) were utilized. Hypoxanthine, potassium oxonate, and sodium urate were purchased from Sigma (USA), and uric acid assay kits were obtained from Wuhan Elabscience Biotechnology Co., Ltd. (China). Additional materials used in the study included quartz micro cuvettes from Tianjin Aoke Lopu Commerce & Trade Co., Ltd. (China), phosphate buffer saline quick-dissolving powder from Wuhan Sevier Biotechnology Co., Ltd. (China), and D101 macroporous adsorption resin from Beijing Solarbio Science & Technology Co., Ltd. (China).

2.2 Animals

Male Wistar rats, aged 6−8 weeks (200−250 g) were obtained from Liaoning Changsheng Biotechnology Co., Ltd. (license No.: SCXK (Liao) 2020-001, certificate No.: YNPZXM202208). All animals were maintained in an SPF-grade laboratory environment at a controlled temperature of (25 ± 1) °C with a 12-h light/dark cycle. All experimental animal procedures adhered to the guidelines of the CAS Animal Ethics Committee, with approval granted on February 28, 2022 (No.: YNPZXM202208).

2.3 Preparation of sunflower receptacles extracts

To prepare the extracts, 4 samples of 100 g each of sunflower receptacles material were taken, and each was dissolved in 500 mL of distilled water using ultrasonication. To each solution, 95% ethanol was added to achieve final concentrations of 20%, 30%, 40%, and 50%. The solutions were then left to stand overnight. After settling, the supernatants were filtered and concentrated to a final concentration of 0.34 g/mL, suitable for dosing. The concentrated extracts were stored at 4 °C until further use.

2.4 Animal model and experimental design

Male Wistar rats weighing (200−250 g) were acclimatized for 10 days before being randomly divided into 8 groups: 1) Blank group: a healthy control group (n = 10) received twice-daily intraperitoneal injections of 0.5 mL/100 g body weight saline for 13 consecutive days. 2) Model group: a hyperuricemia model group (n = 10) was administered twice-daily intraperitoneal injections of a mixture containing 60 mg/mL each of hypoxanthine and potassium oxonate for 13 days. 3–6) Ethanol group (20%, 30%, 40% and 50%): these treatment groups received the same regimen as the model group for inducing hyperuricemia, and from the first day of injection, these groups were treated orally with 0.5 mL/100 g body weight of 0.32 g/mL different sunflower receptacles extract daily for 8 days. 7–8) Allopurinol group, benzbromarone group: these positive control groups also received the same regimen as the model group for inducing hyperuricemia, and from the first day of injection, these groups were also treated orally with 0.5 mL/100 g body weight of allopurinol, or benzbromarone daily for 8 days. According to the literature, the standard value for establishing a hyperuricemic rat model typically ranges from 120 to 180 μmol/L or higher, depending on the species, sex, rearing conditions, and induction methods used[20-21]. In this study, after modeling, the serum uric acid level in hyperuricemic rats increased to 136.12 μmol/L, more than twice that of the control group. Therefore, under the experimental conditions, the hyperuricemia model is considered to have been successfully established[20-21]. On the 6th day post-initial injection, the model and all treatment groups received an intra-articular injection of 100 μL sodium urate (30 mg/mL) into the right knee joint. Joint swelling was measured at 0, 2, 4, 6, 12, and 24 h post-injection using a caliper to assess the extent of inflammation. On day 7, animals were fasted with water *ad libitum* and placed in metabolic cages to collect 24-h urine samples. These samples were then centrifuged at 4 000 r/min at 4 °C, the supernatant was aliquoted and stored at −80 °C. One aliquot was used for uric acid analysis, while others were kept for future use. On day 8, 1 h after the last treatment, animals were euthanized; blood samples were collected and centrifuged at 4 000 r/min at 4 °C, with the supernatant aliquoted and stored at −80 °C. Kidneys, liver, and joints were harvested and fixed in 10% formalin for subsequent histological examination using hematoxylin and eosin (H&E) staining. This protocol ensured comprehensive data collection from both biochemical and histological analyses, providing insights into the effects of treatments on hyperuricemia and associated tissue inflammation.

2.5 Translation for LC-MS analysis of 30% ethanol extract from sunflower receptacles

A total of 20 g of sunflower receptacles were sieved through a 40-mesh screen and immersed in 200 mL of 30% ethanol solution for 1 h. The mixture was then refluxed twice, each time for 2 h[22]. After extraction, the filtrates were combined and concentrated by rotary evaporation at 60 °C. The concentrated extract was freeze-dried, packaged, and stored in a desiccator. For the analysis, 0.5 g of the dried extract was dissolved in 1 mL of 50% methanol[23]. The solution was vortexed for 10 min and sonicated for another 10 min. Subsequently, 10 μL of the supernatant was taken for LC-MS analysis[24].

2.6 Virtual batch docking and machine learning affinity prediction

The receptor protein was constructed based on the bovine XOR enzyme (PDB ID: 3BDJ)[25], which consists of 1 332 residues. Using MODELER 10.1[26-27], homology modeling of the human XO was performed to include missing residues and structural domains. AlphaFold2 was also utilized for human XO modeling, and the Ramachandran plot results of the 2 structure were in Fig. S1. We chose the homology-modeled structure for its higher percentage of residues in the most favored regions (91.6%) and fewer in the additional allowed regions (8%). This modeled structure of 3BDJ was then saved as a PDB file and converted to pdbqt format using Open Babel[28] to transform small molecule SMILES formats into pdbqt format for the ligands. Molecular docking was carried out using AutoDock Vina 1.2.0[29], targeting the molybdenum cofactor[30] (MoCo) site within the XO crystal, which is the active site for substrate inhibition. The docking box was

set with dimensions of 30.0 Å × 33.75 Å × 21.0 Å and center coordinates of x = −22.708, y = 0.066, and z = −9.541. Following the identification of flavonoid small molecules *via* LC-MS[31], batch molecular docking was performed on 16 small molecules along with their target protein. The affinity between these active small molecules and XO was subsequently scored using the BatchDTA[32] model, which assesses drug-target interactions. This approach enabled a comprehensive evaluation of potential inhibitors based on their predicted interaction strength with the target enzyme.

2.7 Inhibitory effects of total extracts of sunflower and four anthraquinone compounds on XO

Using a D101 macroporous resin column with 30% ethanol to extract and purify sunflower extracts[33], the obtained total sunflower extracts were used in this study. The reaction system consisted of xanthine, XO, inhibitors, and buffer solutions. The experiment used 1/15 mol/L PBS as the reaction system buffer, 1/15 mol/L PBS to dilute xanthine, and 1/5 mol/L PBS to dilute XO to a concentration of 0.02 U/mL, while the xanthine reaction concentration was diluted to 0.5 mmol/L. According to the standard curve, different concentrations of inhibitors were prepared. The concentrations of aloe-emodin solution were 102.4, 204.7, 409.5, 819.0, and 1 637.9 μmol/L; the concentrations of emodin solution were 25.8, 51.7, 103.4, 206.8, and 413.6 μmol/L; the concentrations of chrysophanol solution were 90.9, 450, 521, 759, and 1 921.9 μmol/L; the concentrations of rhein solution were 42, 84, 174, 345, and 693 μmol/L. The concentrations of the total sunflower extract solution were 43.5, 87, 175, 350, and 700 μg/mL[34]. The reaction was carried out at a constant temperature of 25 °C, and after 25 min, the absorbance at 290 nm was measured using a UV spectrophotometer due to the characteristic absorption peak of uric acid at 290 nm[35]. The inhibition rate was calculated using the following formula:

$$\text{Inhibition rate}\ (\%) = \frac{1-(A_1-A_2)}{A_3-A_4} \times 100^{[36]} \quad (1)$$

Where, A_1 was absorbance at 290 nm, system containing inhibitor, xanthine, and XO; A_2 was absorbance at 290 nm, system containing inhibitor and xanthine; A_3 was absorbance at 290 nm, system containing xanthine and XO; A_4 was absorbance at 290 nm, system containing only xanthine.

2.8 Study of inhibition mechanism using gaussian accelerated MD simulations

MD simulations were conducted for 3 major molecules: quercetin, apigenin 7-glucoside, and rutin. Allopurinol, recognized as an effective inhibitor of XO, was used as a control in this study, while an apo protein served as a negative control. Conventional MD analyses of the 5 model systems were performed using the cuda module in Amber22[37] (University of California, San Francisco, CA, USA). The protein, ligand, and water molecules were parameterized using the force fields ff14SB[38], GAFF2[39], and TIP3P[40] in Amber22, respectively. A suitable amount of Na^+ was added to neutralize the system[41]. All bonds involving hydrogen atoms were constrained using the SHAKE algorithm[42]. Periodic boundary conditions (PBC) were applied to the 3 systems to prevent edge effects. The initial structures for GaMD[43] simulations were obtained from well-equilibrated structures of cMD simulations. In this study, dual potential boosts were applied to the GaMD simulations, with boosts applied to the total potential energy and dihedral potential energy (igamd = 3)[44]. Potential energy boost helps accelerate the sampling of conformational space by lowering the energy barriers in the entire potential energy landscape, and dihedral potential energy boost is specifically applied to the dihedral angles of the molecular system, focusing on enhancing sampling around the dihedral degrees of freedom, which are often the slow degrees of freedom in biomolecular simulations. By doing so, it enables faster transitions between different conformational states that are separated by dihedral rotations. The dual potential boost parameters were defined by a preceding 50 ns cMD simulation. Subsequently, multiple GaMD simulations were performed for the 5 systems, saving coordinates every 10 ps, with a total simulation time of 500 ns for each system. The GaMD trajectories were used for subsequent analyses. Trajectory analyses, including root mean square deviation (RMSD)[45], radius of gyration (Rg)[46], solvent-accessible surface area (SASA)[47], and root mean square fluctuation (RMSF)[48], were calculated using the Cpptraj module[49] of Amber22. Principal component analysis (PCA)[50], a widely used dimensionality reduction method describing the concerted motion of the entire protein, was also calculated using Cpptraj. The ddtpd software from Lu was used to construct free energy landscapes (FELs) to identify dominant conformations and their corresponding energy barriers[51].

2.9 Markov analysis

In this study, MSMs[52] were constructed using PyEMMA 2.5.7[53] following the workflow described below. First, the system was featurized by selecting the regions with the lowest RMSD from the MD trajectories, and segments 875−885 and 1 261−1 268 were chosen as region_1 and region_2, respectively. Next, time-lagged independent component analysis (TICA)[54] was used to reduce the spatial dimensions to 2 collective coordinates. This technique retained 95% of the dynamic variance of the original data and identified the slowest modes in the feature space by maximizing the autocorrelation of the simplified coordinates. The conformations of each system were then clustered into microstates using the k-means algorithm. A sliding window method was applied to count the number of transitions between pairs of microstates within an appropriate lag time, constructing a transition count matrix. The Bayesian MSM estimator was then used to obtain the transition probability matrix. The timescales were investigated to determine when the system becomes Markovian. The Chapman-Kolmogorov test[55] was employed to assess the validity of the Bayesian Markov model, showing an almost perfect agreement between the estimated transition probabilities from the MD data and the predictions from the MSM, indicating the MSM's validity. Subsequently, the Perron cluster cluster analysis (PCCA)[56] algorithm was used to further divide these microstates into macrostates. Finally, transition path theory (TPT)[57] was utilized to elucidate the transitions between these macrostates.

2.10 Data analysis

GaMD trajectories were used for subsequent analyses. RMSD, Rg, SASA, RMSF, and PCA were calculated using the Cpptraj module in

Amber22. Free energy landscapes were constructed from the GaMD trajectories using the ddtpd software developed by Lu to characterize dominant conformational states and the associated energy barriers. Unless otherwise stated, the same data-processing and analysis workflow was applied to all systems to ensure consistency and comparability.

3. Result and discussion

3.1 Determination of the optimal ethanol concentration for extracting sunflower receptacles

3.1.1 Joint swelling test

Sunflower receptacles were reflux-extracted using 20%, 30%, 40%, and 50% ethanol solutions. The 4 ethanol extract groups were evaluated alongside the blank group, the model group, and the allopurinol and benzbromarone groups. After intra-articular injection of sodium urate, the degree of joint swelling in rats over time is shown in Fig. 2. After 24 h, the joint swelling in rats treated with extracts from 20% and 50% ethanol-extracted sunflower discs were (34.78 ± 0.13)% and (31.62 ± 0.25)%, respectively, indicating poorer anti-swelling effects. For the 30% ethanol group, the joint swelling was significantly reduced to (21.74 ± 0.12)% after 24 h, much lower than the model group at (36.36 ± 0.12)%, and also lower than the allopurinol and benzbromarone groups, demonstrating a better anti-swelling effect. Additionally, the 40% ethanol group showed a swelling of (24.90 ± 0.23)%, which was also comparatively effective.

3.1.2 Serum uric acid and urinary uric acid levels

Serum uric acid is an important measure of hyperuricemia, and urinary uric acid levels are also related to the concentration of uric acid in the blood. The serum uric acid levels in each rat group are shown in Fig. 3A, and the urinary uric acid levels in Fig. 3B. The blank group had a serum uric acid level of (62.21 ± 13.89) μmol/L.

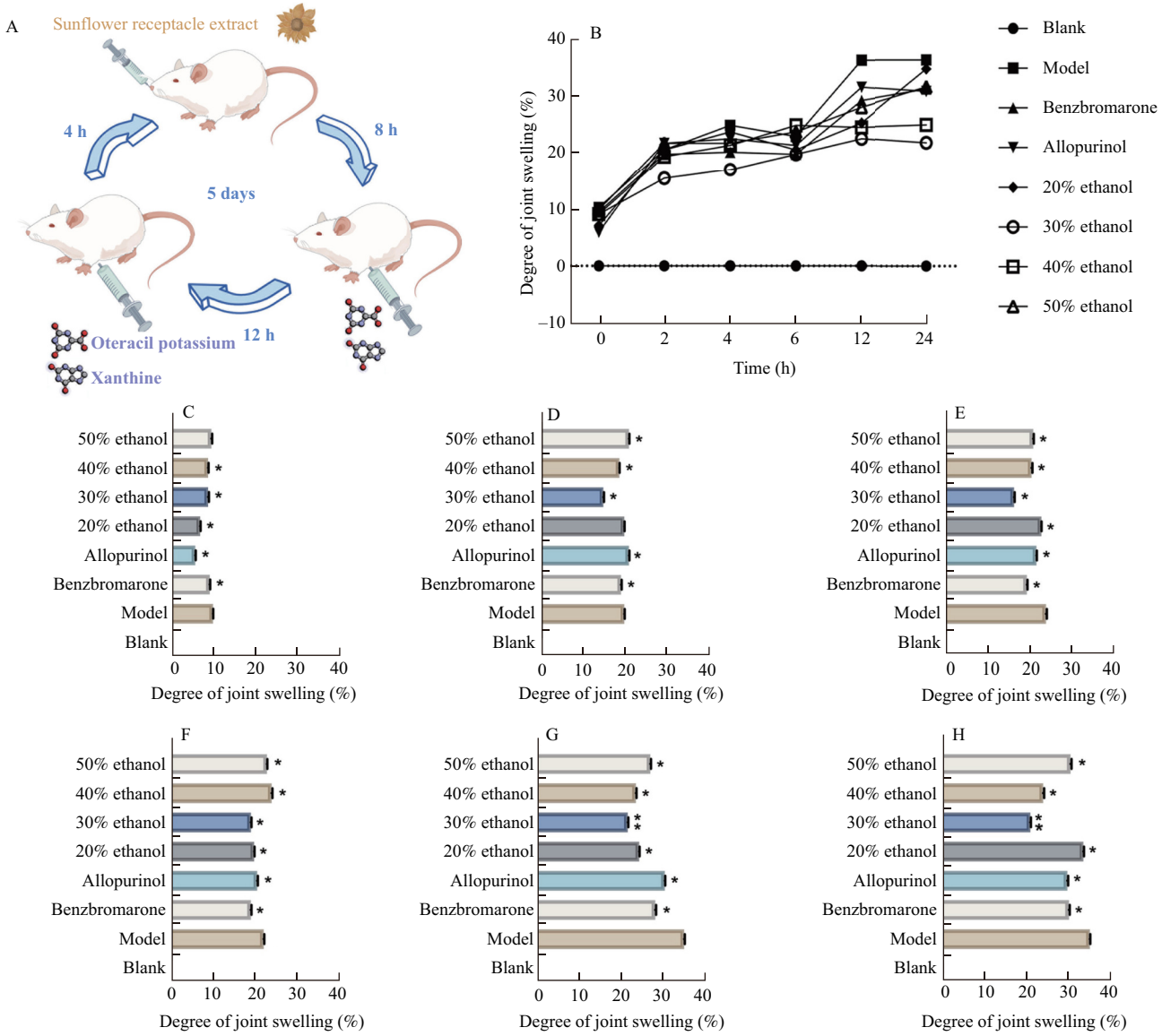

Fig. 2 Changes in joint swelling percentage in different rat groups. (A) Schematic diagram of the experimental procedure. (B) Dynamic changes in the degree of joint swelling over time in each group. Comparison of the degree of joint swelling among groups at (C) 0, (D) 2, (E) 4, (F) 6, (G)12, (H) 24 h. Data are presented as mean ± SD. *$P < 0.05$, **$P < 0.01$ *vs.* the Model group at the corresponding time point.

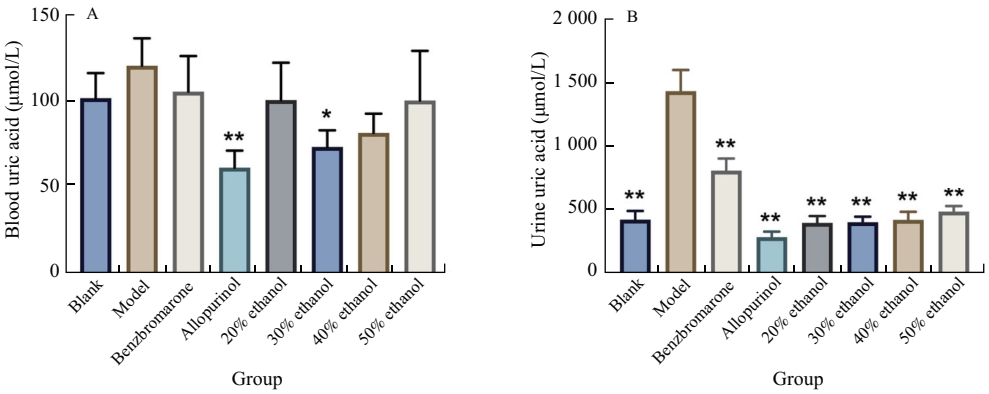

Fig. 3 Serum uric acid concentration levels and urinary uric acid concentration levels in different groups. (A) Serum uric acid concentration levels. (B) Urinary uric acid concentration levels. *$P < 0.05$, **$P < 0.01$ *vs.* Model group.

The model group showed a significantly higher level, confirming the effectiveness of our model; among the treatment groups, the positive control drug allopurinol showed the best reduction in serum uric acid levels, followed by the 30% and 40% ethanol extract groups. The blank group's urinary uric acid level was (433.62 ± 70.00) μmol/L, which was significantly different from the model group ($P < 0.01$), indicating a sharp increase in urinary uric acid after model establishment. All treatment groups showed a significant decrease in urinary uric acid compared to the model group, with the best results seen in the allopurinol and 30% ethanol groups, due to the reduction of blood uric acid levels. The benzbromarone group had higher urinary uric acid levels, possibly due to its mechanism of inhibiting uric acid reabsorption and promoting excretion[58]. By comparing data with the 2 positive control drugs, allopurinol and benzbromarone, the extracts from sunflower receptacles did not increase urinary uric acid, suggesting that their mechanism of treating hyperuricemia might differ from that of benzbromarone and is not based on promoting excretion but rather resembles allopurinol by inhibiting XO to lower uric acid levels.

3.1.3 Drug hepatorenal toxicity

The impact of drugs on liver and kidney function has always been a key focus in drug development. The kidney morphology change grading table for each group is shown in Table S1, and the liver morphology change grading table is in Table S2. Fig. 4 displays the pathological morphology images of the kidneys and livers for each group. Pathological analyses of liver and kidney sections (Fig. 3) reveal that the animal model was successfully replicated with observable changes such as glomerular expansion and degeneration and dilation of renal tubules within the kidneys; the allopurinol and benzbromarone groups showed better results, reducing ($P < 0.05$) the extent of kidney damage and providing some protection of kidney morphology and function; the 30%, 40%, and 50% ethanol extract groups significantly alleviated ($P < 0.01$) kidney damage and effectively protected kidney morphology and function, performing better than the positive drug control groups. Compared to the normal group, no significant morphological differences were observed in the liver cells of the model group, indicating that the modeling drugs have not significantly altered liver cell morphology. No significant changes were observed in liver cells in the 30% ethanol extract group, but the 40% and 50% ethanol extract groups caused liver cell loosening and deformation. Currently, the administration period is 7 days; to further evaluate hepatorenal toxicity, longer-term toxicity studies are necessary[59].

Animal studies have proven that flavonoid extracts from sunflower receptacles are effective in treating hyperuricemia, particularly the 30% ethanol extract from sunflower receptacles, which not only reduces joint swelling, serum uric acid, and urinary uric acid levels but also protects the kidneys without harming the liver. Subsequently, the primary drug molecules and specific mechanisms of the 30% ethanol extract of sunflower receptacles for treating hyperuricemia were further explored.

3.2 LC-MS, active molecule virtual screening, and experimental identification

LC-MS identified 16 flavonoid molecules present in the 30% ethanol group. According to the results from animal experiments, these extracts did not increase urinary uric acid levels but instead reduced serum uric acid levels. This suggests that their mechanism for treating hyperuricemia may differ from the mechanism of benzbromarone, as benzbromarone promotes the excretion of uric acid. Instead, their mechanism is more similar to that of allopurinol, which lowers uric acid levels by inhibiting XO. Therefore, it is hypothesized that the primary mechanism of action in treating hyperuricemia involves the inhibition of XO. Therefore, molecular docking and the machine learning affinity evaluation method, BatchDTA, were employed to assess their potential affinity with XO, aiming to identify competitive inhibitors, as shown in Table 1.

The top 4 ranked molecules were validated and their IC_{50} values were tested, the results were shown in Fig. 5. Among the sunflower receptacle flavonoids, quercetin showed the best inhibitory effect with an IC_{50} of 45.35 μmol/L. The overall inhibitory effect of total flavonoids was affected by some molecules with poor bioactivity, showing a higher IC_{50} of 441.8 μg/mL. Additionally, apigenin 7-glucoside is a newly discovered XO inhibitor previously unreported, with an IC_{50} of 444.2 μmol/L. In comparison, the positive control drug, allopurinol,

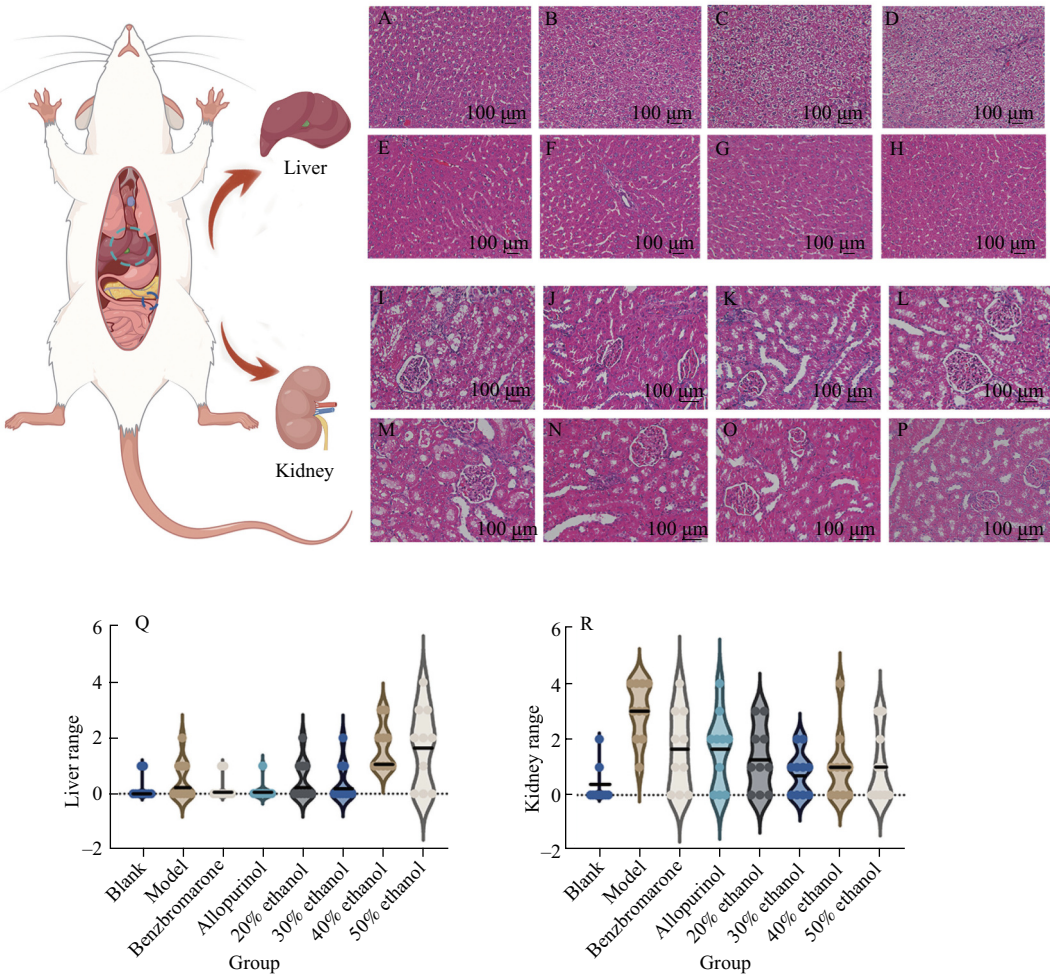

Fig. 4 Pathological morphology images of the kidneys and livers for each group. (A, I) 20% ethanol group; (B, J) 30% ethanol group; (C, K) 40% ethanol group; (D, L) 50% ethanol group; (E, M) Benzbromarone group; (F, N) Allopurinol group; (G, O) Blank group; (H, P) Model group in liver and kidney. (Q) Liver grading chart; (R) Kidney grading chart.

demonstrated a superior inhibitory effect with an IC_{50} of 22.78 μmol/L (Fig. S2). These findings highlight the potential of small-molecule compounds derived from sunflower head flavonoids as promising anti-hyperuricemic agents. Although their efficacy is lower than that of allopurinol, these natural compounds offer a valuable starting point for further optimization and development as lead molecules for the treatment of hyperuricemia.

3.3 *Gaussian accelerated MD simulation*

To further investigate the mechanism of quercetin inhibiting XO, MD simulations were performed based on the molecular docking results. Rutin, apigenin 7-glucoside, and the positive control drug allopurinol, along with the apo protein, were used as control groups in a total of five systems. The initial docking structures used are shown in Fig. 6. Both apigenin 7-glucoside and quercetin interact with multiple residues through hydrogen bonds and stacking forces, whereas rutin mainly forms hydrogen bonds and involves fewer residues that contribute to binding strength, also showing some unfavorable interactions. Allopurinol primarily binds to XO through hydrogen bonds as well, and additionally, it has a π-anion interaction with ASP872.

3.3.1 *Structural stability and dynamics properties*

The RMSD illustrates the deviation of the complex from its initial conformation, with increases and fluctuations in RMSD indicating conformational changes during the simulation. Quercetin shows a more stable RMSD, indicating better protein stability (Figs. 7A and D). The solvent accessible surface area (SASA) describes the hydrophilicity of the protein; a smaller SASA indicates a more hydrophobic protein. The Rg reveals the compactness of the complex, with a smaller Rg indicating a more compact protein. The SASA (Figs. 7B and E) and Rg (Figs. 7C and F) of the quercetin group are smaller than those of the apo protein, similar to, and even better than, allopurinol.

As shown in Fig. 7G, the RMSF is lower, also indicating that quercetin can stabilize XO. In contrast, the poorer inhibitors, rutin and apigenin 7-glucoside, exhibit higher RMSF, indicating instability at multiple sites. Additionally, by analyzing the ligand RMSD, it

is observed that quercetin and allopurinol are stably bound at the initially docked active site, resulting in low RMSD. Poorer inhibitors like rutin deviate from the docked active site, which likely leads to decreased inhibitory effects (Fig. 7H).

3.3.2 Binding energy and energy landscape

The results of the molecular mechanics Poisson-Boltzmann surface area (MM-PBSA) are presented in Table 2. This method evaluates the binding free energy between the ligand and the target enzyme, providing a quantitative measure of the interaction strength. Quercetin exhibited a binding free energy of (−17.13 ± 4.02) kcal/mol, indicating a stronger binding affinity than allopurinol, which showed a binding free energy of (−5.74 ± 3.21) kcal/mol.

Fig. 8 displays the MM-PBSA energy contribution and the analysis of the number of hydrogen bonds for 4 systems. Quercetin forms a higher number of hydrogen bonds and exhibits a lower binding free energy, indicating stronger binding affinity, consistent with experimental results.

A PCA of all the Cα atoms, conducted for the 5 systems, is illustrated in Fig. 9. The free-energy landscape was constructed using the PCA results, identifying low-energy stable representative conformations. The energy landscape of quercetin distinctly shows differences between

Table 1
Data table of the identified molecule.

Identification Name	Structure	Neutral mass (Da)	Observed (*m/z*)	Error (× 10^{-6})	MS+ and elevated energy (MSE, *m/z*)	BatchDTA affinity	Autodock vinabind energyc (kcal/mol)
Quercetin	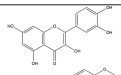	302.042 65	301.037 1	5.8	301.036 83, 151.004 04, 285.038 21, 125.024 65, 107.013 27	6.221 169 949	−9.8
Acacetin	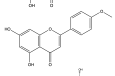	284.068 47	329.067 2	1.5	151.003 99, 241.157 67, 269.044 51	6.501 067 638	−9.4
Rutin		610.153 38	609.141 6	−7.4	463.088 41, 301.035 16, 127.076 84	6.051 778 793	−9.5
Apigenin 7-glucoside	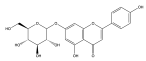	466.121 3	491.118 5	−2.1	267.159 45	6.050 847 53	−9.1
Mikanin	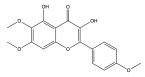	344.089 6	343.083 6	3.8	167.035 41, 151.004 04, 133.029 85, 120.996 33, 301.036 83, 313.035 98, 328.053 33, 343.210 84	6.593 221 188	−8.5
Genistin	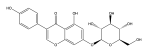	432.105 65	477.103 6	−0.6	353.088 61, 310.088 69	6.551 994 801	−8.3
Cynaroside	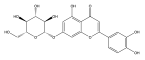	448.100 56	493.099 6	1.6	287.021 59	7.013 622 761	−7.8
Daidzin	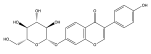	461.110 73	461.109 7	1.7	251.092 68	6.714 657 307	−7.8
Nevadensin	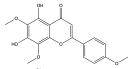	344.089 6	343.083 6	3.8	315.19417, 313.23689, 313.03725	6.730 061 531	−7.6
Tricin 5-glucoside	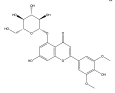	492.126 78	491.117 2	−4.7	323.077 60, 167.035 50, 108.021 88	6.684 195 995	−7.6
Quercetin-3′-glucoside	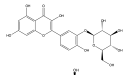	464.095 48	463.088 9	4.5	301.036 26, 335.020 81, 151.004 33, 107.013 76, 273.035 95	6.095 970 154	−8.1
Isorhamnetin 3-*O*-glucoside	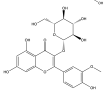	478.111 13	477.103 6	−0.6	353.088 61, 179.035 85, 173.046 48, 161.025 16	6.538 193 226	−7.4
Kaempferol 3-*O*-rhamnoside		432.105 65	477.103 6	−0.6	285.182 68, 255.066 27	6.700 454 712	−7
Isoquercetin	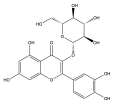	464.095 48	463.088 6	0.9	191.056 64, 301.035 99, 151.003 60, 125.024 28	6.103 028 297	−7.5
Tambulin	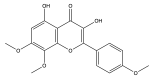	344.089 6	343.083 6	3.8	298.013 71, 315.194 17	6.576 121 807	−7
Astragalin	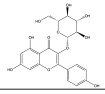	448.100 56	493.099 6	1.6	283.156 71	6.237 398 624	−7.2

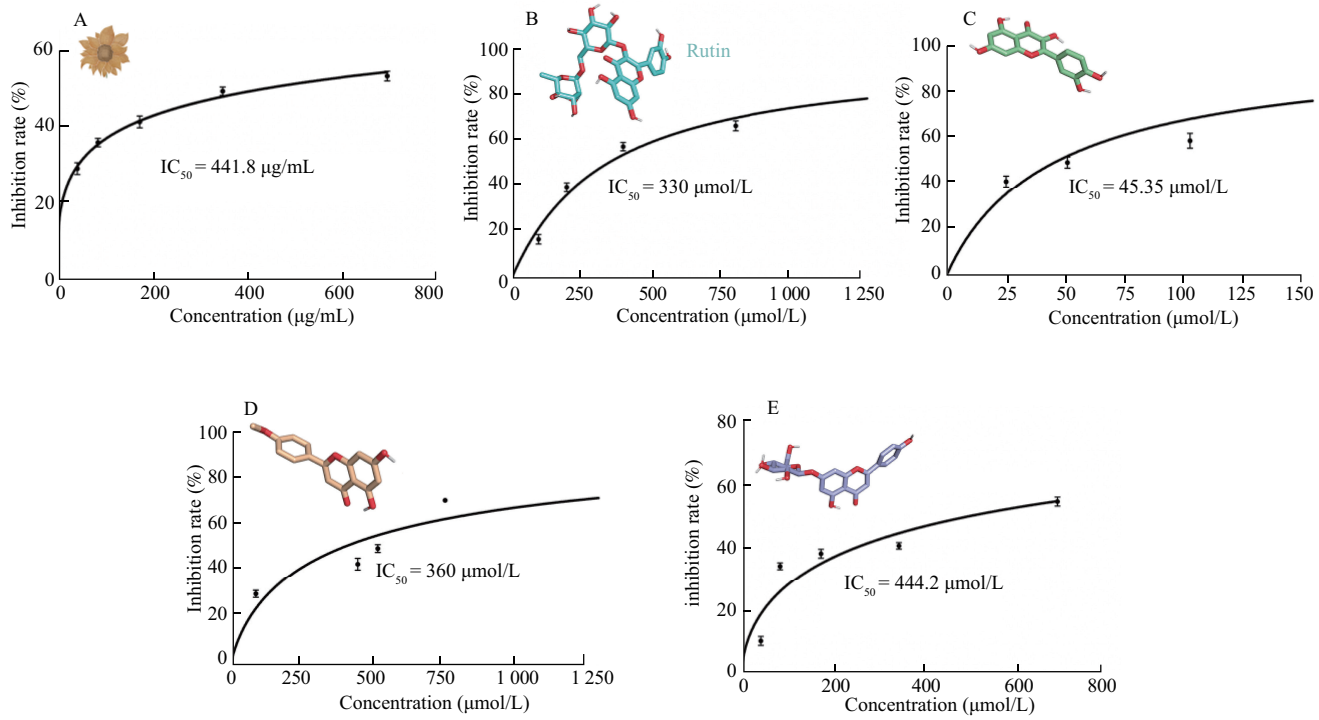

Fig. 5 IC_{50} values for the top four molecules and total flavonoids from sunflower receptacles. (A) Total flavonoid extract from sunflower receptacles; (B) Rutin; (C) Quercetin; (D) Acacetin; (E) Apigenin 7-glucoside.

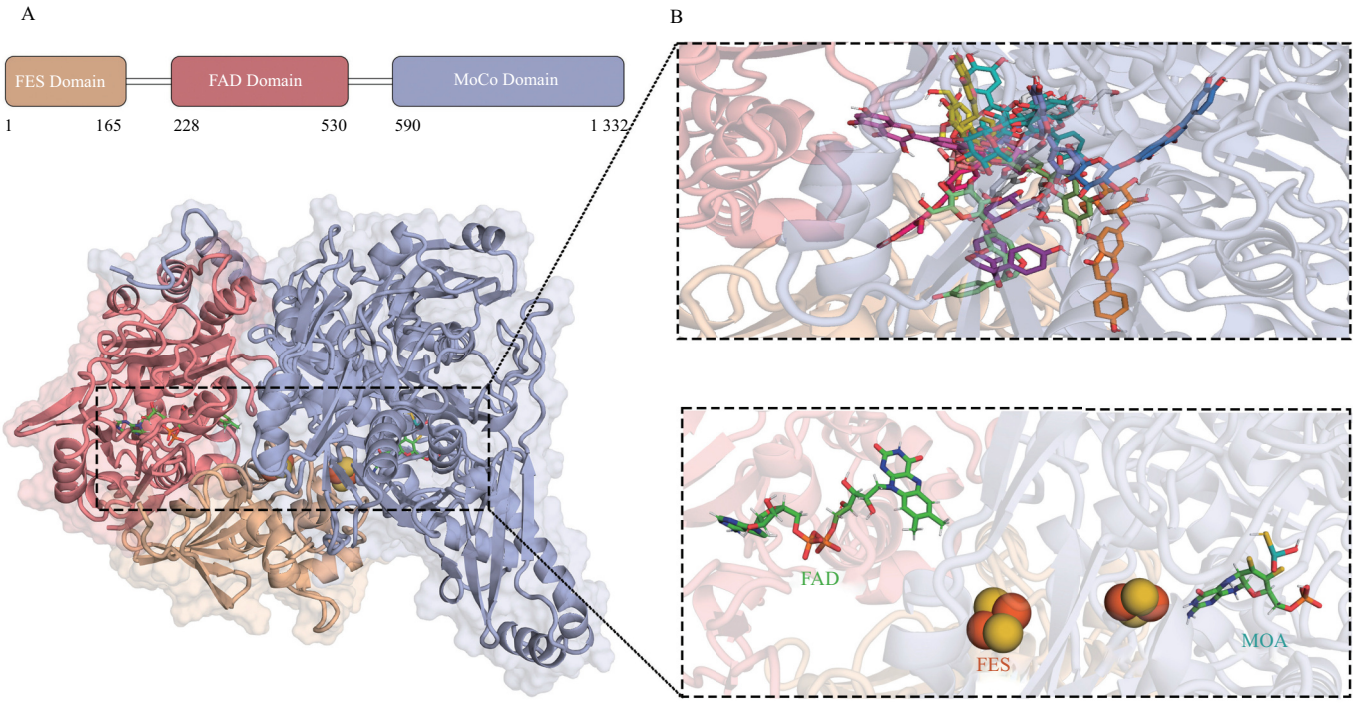

Fig. 6 Molecular docking images of MD systems. The FES, FAD, and MoCo domains are shown in distinct colors. Green lines represent conventional hydrogen bonds, purple lines indicate π-π stacked and π-π T-shaped interactions, pink lines show π-alkyl interactions, and orange lines show π-anion interaction. (A) Structural domain of XO. (B) Structural diagram of XO. (C) Docking result of apigenin 7-glucoside. (D) Docking result of rutin. (E) Docking result of quercetin. (F) Docking result of allopurinol.

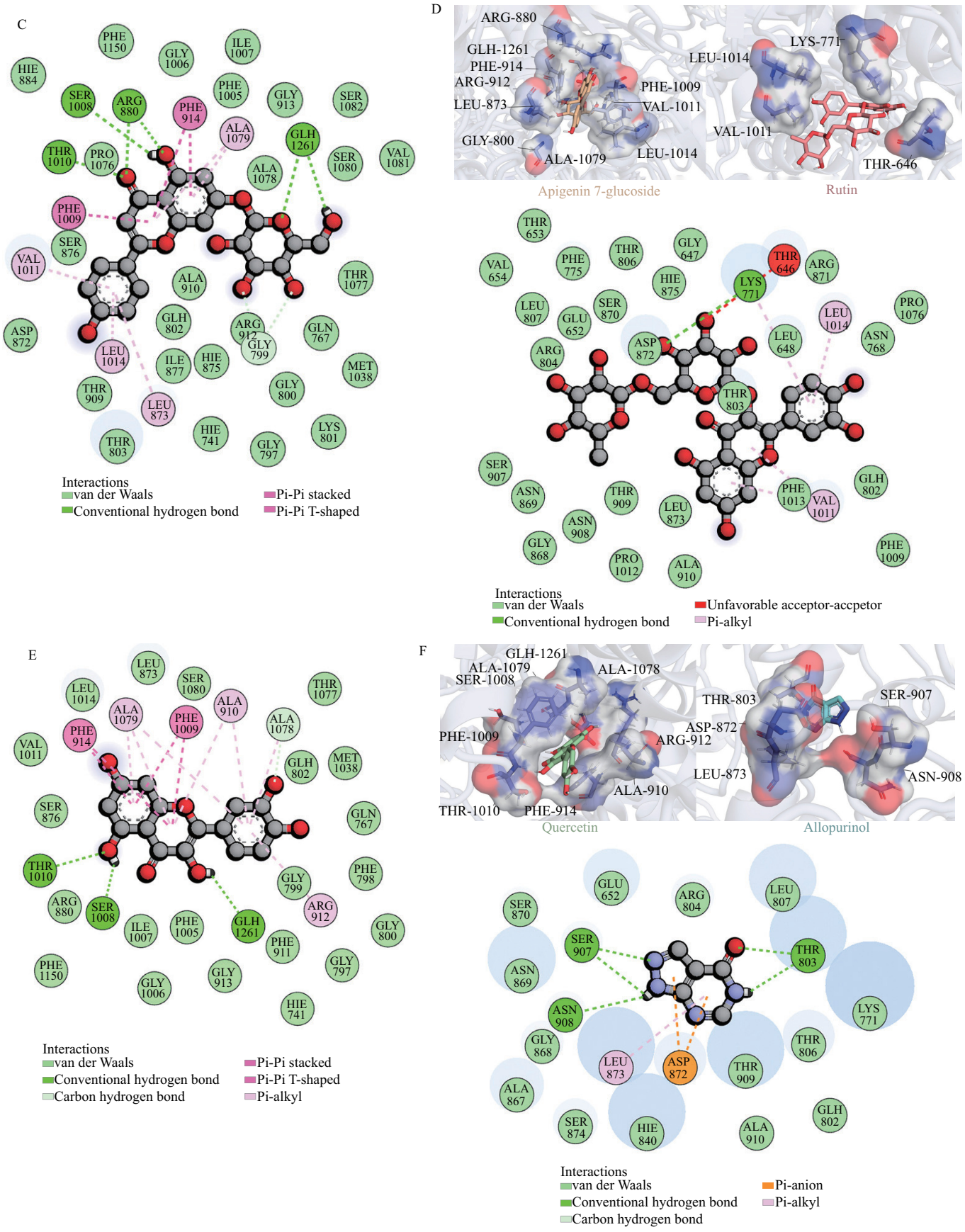

Fig. 6 (*Continued*)

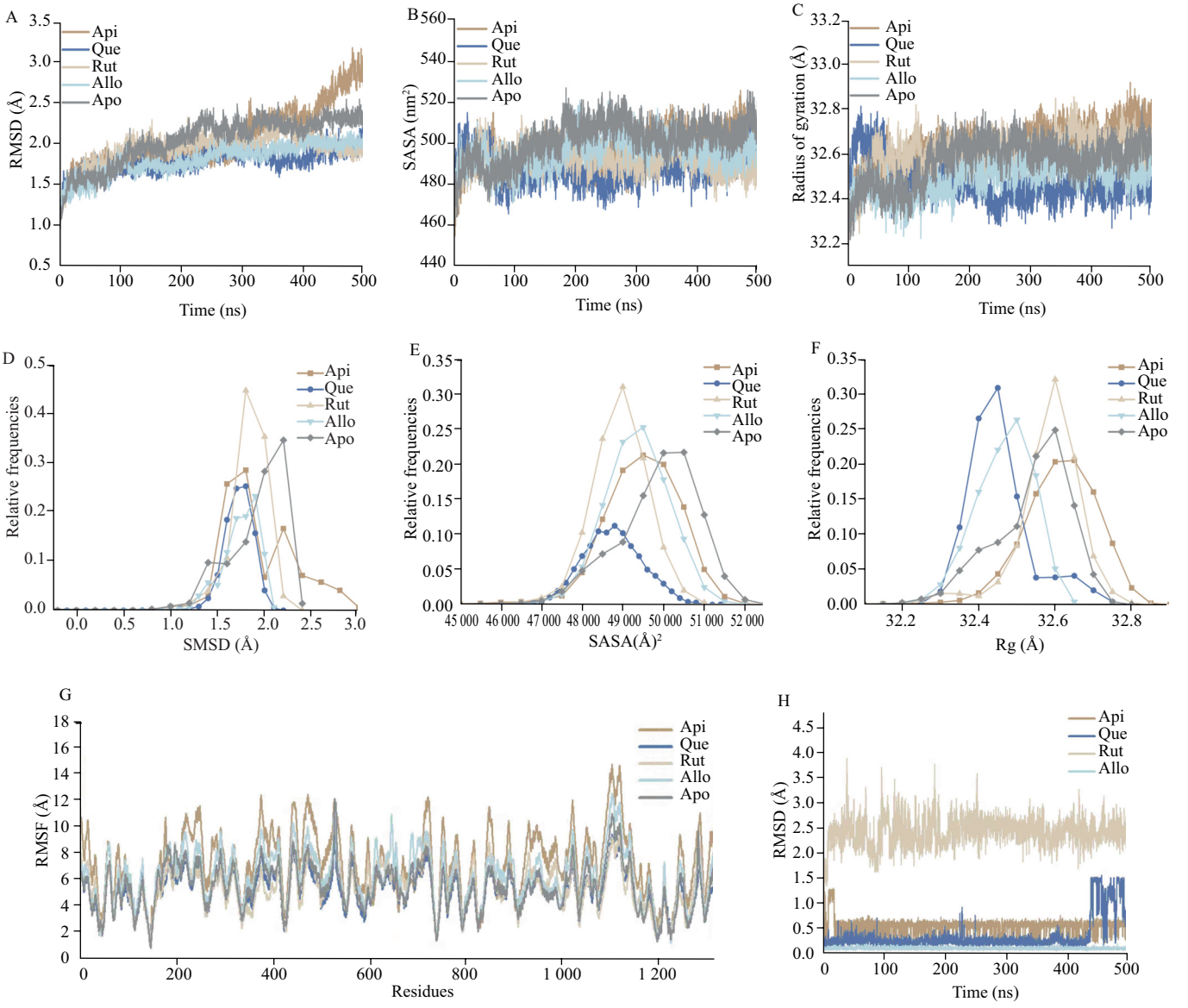

Fig. 7 Structural stability analysis of 5 systems. (A) Time evolution of RMSD from their initial structures for the 5 systems. (B) SASA during a 500-ns MD simulation. (C) Rg for 3 systems during a 500-ns MD simulation. (D) RMSD relative frequency distribution, showing the range of RMSD values for each system. (E) SASA relative frequency distribution, showing the range of RMSD values for each system. (F) Rg relative frequency distribution, showing the range of RMSD values for each system. (G) RMSF for 3 systems. (H) Time evolution of RMSD for 4 inhibitory small molecules. Api, apigenin 7-glucoside; Que, quercetin; Rut, rutin; Allo, allopurinol, Apo, apo protein.

Table 2
Results of the MM-PBSA.

System	Apigenin 7-glucoside	Quercetin	Rutin	Allopurinol
ΔEvdW (van der Waals interaction energy)	−36.46 ± 2.79	−35.24 ± 2.41	−42.20 ± 4.02	−21.36 ± 0.32
ΔEele (electrostatic interaction energy)	−21.42 ± 3.72	−23.40 ± 6.64	−41.04 ± 3.29	−20.21 ± 0.78
ΔGgas (gas-phase free energy)	−57.88 ± 2.81	−58.64 ± 6.02	−86.25 ± 3.25	−41.57 ± 4.35
ΔGsolv (solvation free energy)	35.46 ± 3.27	41.51 ± 4.37	72.63 ± 2.58	35.83 ± 3.99
ΔGtotal	−22.42 ± 2.63	−17.13 ± 4.02	−13.62 ± 1.02	−5.74 ± 3.21

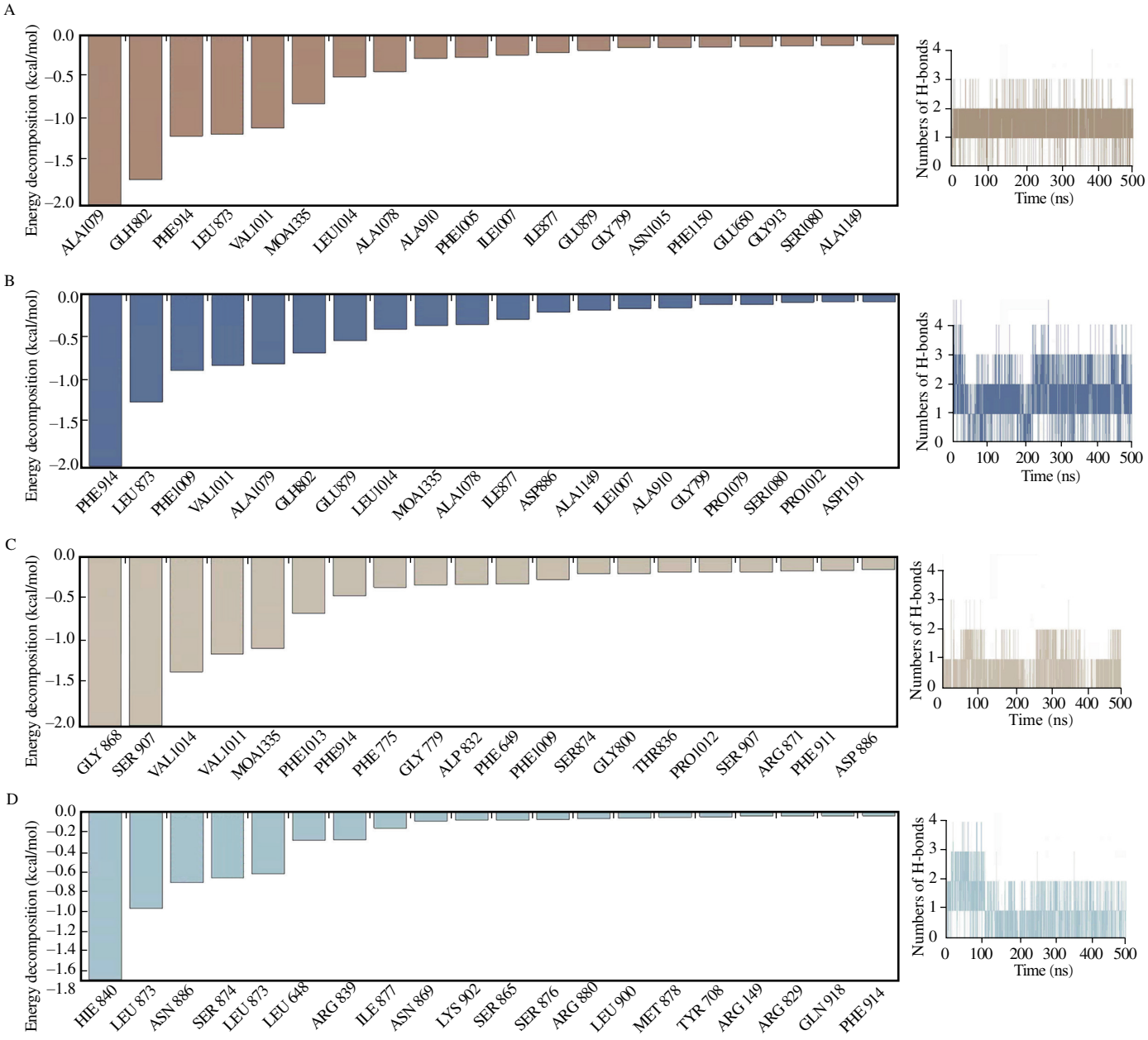

Fig. 8 MM-PBSA energy contribution and hydrogen bonds. (A) Apigenin 7-glucoside. (B) Quercetin. (C) Rutin. (D) Allopurinol.

inhibitory and non-inhibitory states, with an energy landscape pattern similar to that of allopurinol. Rutin and the apo protein exhibit similar energy landscapes (Figs. 9C and D), with no clear inhibitory states, distributing smoothly across the conformational space.

3.3.3 MSM

To further explore the dynamic mechanisms of conformational transitions, an MSM analysis was conducted for 3 systems: allopurinol, quercetin, and the apo protein, as shown in Fig. 10. The state space of quercetin and the positive control allopurinol are similar, clearly showing differences between inhibitory and non-inhibitory states, with a high flux into the inhibited state and shorter transition times. However, the transition from the inhibited to non-inhibited state takes longer, indicating that this process is less likely to occur. Notably, for allopurinol (Fig. 10A), transitioning from a non-inhibited to an inhibited state (State1) takes only 0.01 and 0.03 ns; whereas for quercetin (Fig. 10B), moving from a non-inhibited to an inhibited state (State2) requires 0.7 and 1.23 ns; this suggests that in terms of the probability of conformational transitions, allopurinol is still superior to quercetin, indicating that there is room for improvement in quercetin. As for the apo protein group, the frequent transitions among multiple conformations correlate with the smooth energy landscape obtained from PCA, showing no distinct advantageous conformation.

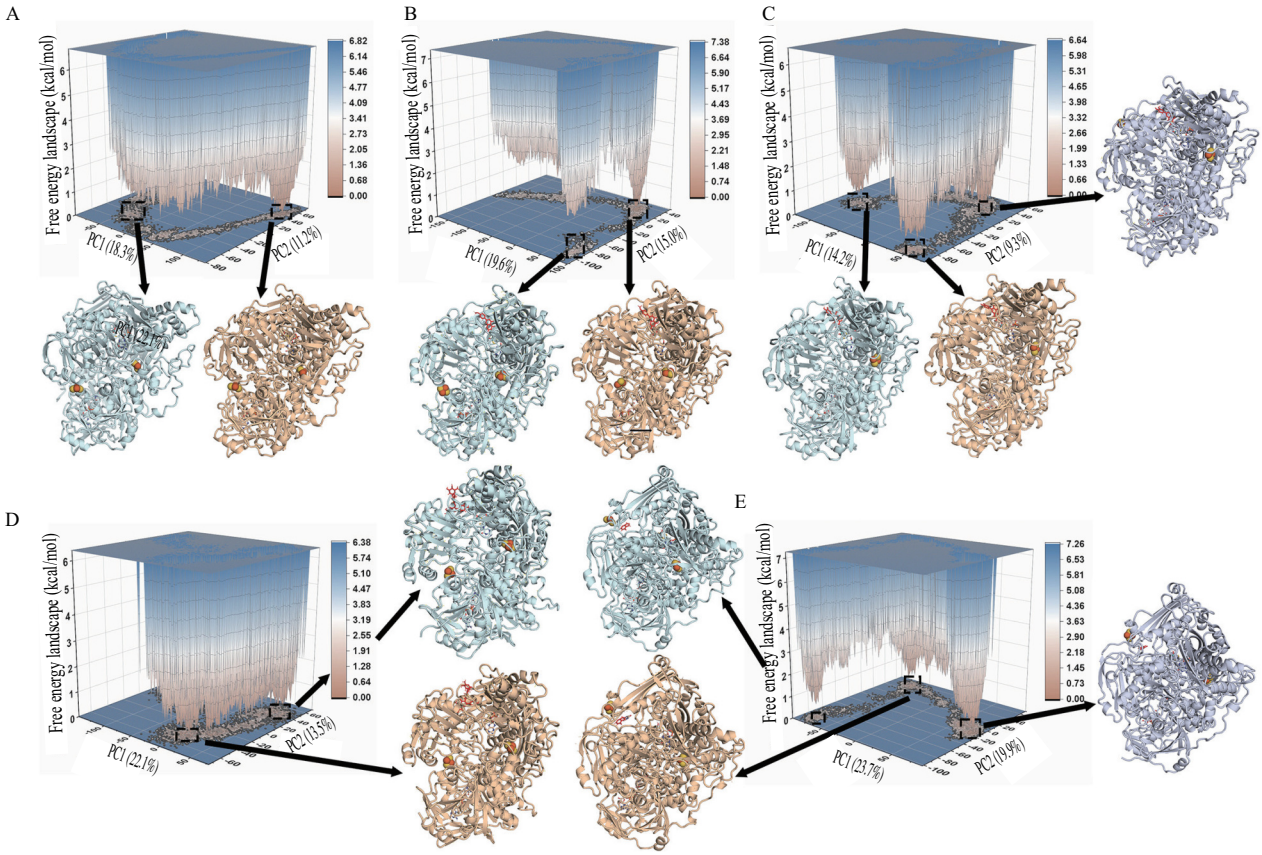

Fig. 9 FELs of 5 systems. (A) Apigenin 7-glucoside; (B) Quercetin; (C) Apo protein; (D) Rutin; (E) Allopurinol.

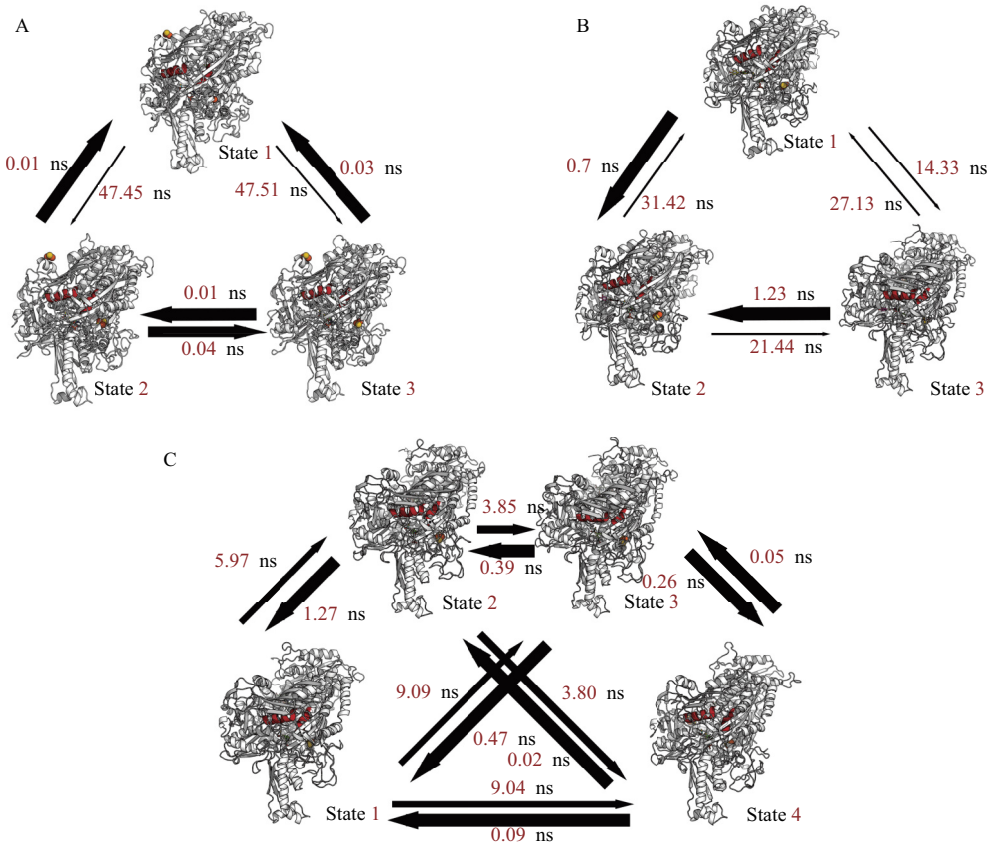

Fig. 10 MSM of 3 systems. (A) Allopurinol; (B) Quercetin; (C) Apo protein.

4. Conclusion

This study explored the potential of flavonoid molecules from sunflower receptacles in treating hyperuricemia. Animal experiments identified 30% as the optimal ethanol extraction concentration, demonstrating good effects in reducing joint swelling, serum uric acid, and urinary uric acid levels, while also providing protection to the liver and kidneys. Using LC-MS, 16 flavonoid compounds were identified, and through virtual screening and validation, quercetin from sunflower receptacle flavonoid was found to be an effective inhibitor of XO with an IC_{50} of 45.35 μmol/L. There is a novel discovery that apigenin 7-glucoside inhibits XO activity. Subsequently, MD simulations and MSMs demonstrated that the mechanism of quercetin's inhibition of XO is similar to that of allopurinol.

These findings highlight that flavonoid molecules from sunflower receptacles, especially quercetin, play a critical role in treating gout. This study provides evidence for the use of these natural compounds in medicine, and it demonstrates the feasibility of a combination of computational methods and experiments to identify and analyze potential drug candidates from plants.

Competing interests

All the authors have declared no conflict of interest.

Acknowledgement

This research was funded by the Science and Technology Development Plan Project of Jilin Province, China (20230204044YY).

Appendix A. Supplementary data

Supplementary data associated with this article can be found, in the online version, at http://doi.org/10.26599/FSHW.2024.9250408.

References

[1] G. Desideri, G. Castaldo, A. Lombardi, et al., Is it time to revise the normal range of serum uric acid levels? Eur. Rev. Med. Pharmacol. Sci. 18 (2014) 1295-1306.

[2] S. Zhang, Y. Wang, J. Cheng, et al., Hyperuricemia and cardiovascular disease, Curr. Pharm. Des 25 (2019) 700-709. https://doi.org/10.2174/1381612825666190408122557.

[3] H. Yanai, H. Adachi, M. Hakoshima, et al., Molecular biological and clinical understanding of the pathophysiology and treatments of hyperuricemia and its association with metabolic syndrome, cardiovascular diseases and chronic kidney disease, Int. J. Mol. Sci. 22 (2021) 9221 https://doi.org/10.3390/ijms22179221.

[4] C.M. van Durme, M.D. Wechalekar, R.B. Landewé, et al., Non-steroidal anti-inflammatory drugs for acute gout, Cochrane Database Syst. Rev. 12 (2021) Cd010120. https://doi.org/10.1002/14651858.CD010120.pub3.

[5] P.I. Hair, P.L. McCormack, G.M. Keating, Febuxostat, Drugs 68 (2008) 1865-1874. https://doi.org/10.2165/00003495-200868130-00006.

[6] Q. Li, X. Li, J.S. Kwong, et al., Diagnosis and treatment for hyperuricaemia and gout: a protocol for a systematic review of clinical practice guidelines and consensus statements, BMJ Open 7 (2017) e014928. https://doi.org/10.1136/bmjopen-2016-014928.

[7] B.V. Zavodovsky, L.E. Sivordova, Cardiovascular safety of non-steroidal anti-inflammatory drugs in chronic inflammatory rheumatic diseases, Ter. Arkh. 90 (2018) 101-106. https://doi.org/10.26442/terarkh2018908101-106.

[8] M.K. Malewska-Kasprzak, A. Permoda-Osip, J. Rybakowski, Disturbances of purinergic system in affective disorders and schizophrenia, Psychiatr. Pol 53 (2019) 577-587. https://doi.org/10.12740/PP/97335.

[9] M. Leigh, D.J. Raines, C.E. Castillo, et al., Inhibition of xanthine oxidase by thiosemicarbazones, hydrazones and dithiocarbazates derived from hydroxy-substituted benzaldehydes, ChemMedChem 6 (2011) 1107-1118. https://doi.org/10.1002/cmdc.201100054.

[10] R. Hille, T. Nishino, Flavoprotein structure, mechanism. 4. Xanthine oxidase and xanthine dehydrogenase, FASEB J. 9 (1995) 995-1003.

[11] S. Zamani, M.R. Naderi, A. Soleymani, et al., Sunflower (*Helianthus annuus* L.) biochemical properties and seed components affected by potassium fertilization under drought conditions, Ecotoxicol. Environ. Saf. 190 (2020) 110017. https://doi.org/10.1016/j.ecoenv.2019.110017.

[12] L.M. Radonic, D.M. Lewi, N.E. Lopez, et al., Sunflower (*Helianthus annuus* L.), Methods Mol. Biol. 1224 (2015) 47-55. https://doi.org/10.1007/978-1-4939-1658-0_5.

[13] N.P. Everett, K.E.P. Robinson, D. Mascarenhas, Genetic engineering of sunflower (*Helianthus Annuus* L.), Bio/Technology 5 (1987) 1201-1204. https://doi.org/10.1038/nbt1187-1201.

[14] K. Wang, H. Cui, K. Liu, et al., Exploring the anti-gout potential of sunflower receptacles alkaloids: a computational and pharmacological analysis, Comput. Biol. Med. 172 (2024) 108252. https://doi.org/10.1016/j.compbiomed.2024.108252.

[15] A. Singh, D.K. Singh, R.N. Kharwar, et al., Fungal endophytes as efficient sources of plant-derived bioactive compounds and their prospective applications in natural product drug discovery: insights, avenues, and challenges, Microorganisms 9 (2021) 197. https://doi.org/10.3390/microorganisms9010197,

[16] S. Kar, K. Roy, How far can virtual screening take us in drug discovery? Expert Opin. Drug Discov. 8 (2013) 245-261. https://doi.org/10.1517/17460441.2013.761204.

[17] K.W. Chen, T.Y. Sun, Y.D. Wu, New insights into the cooperativity and dynamics of dimeric enzymes, Chemi. Rev. 123 (2023) 9940-9981. https://doi.org/10.1021/acs.chemrev.3c00042.

[18] V.T. Duong, Investigation of protein sequence-structure dynamics using bioinformatics, molecular dynamics and machinelearning, University of California, Irvine, 2020.

[19] D.K. Mahapatra, S.K. Bharti, handbook of research on medicinal chemistry: innovations and methodologies, Taylor & Francis, 2017. https://doi.org/10.1201/9781315207414.

[20] M. Li, D. Yang, L. Mei, et al., Screening and characterization of purine nucleoside degrading lactic acid bacteria isolated from Chinese sauerkraut and evaluation of the serum uric acid lowering effect in hyperuricemic rats, PLoS One 9 (2014) e105577. https://doi.org/10.1371/journal.pone.0105577.

[21] F. Hong, A. Zheng, P. Xu, et al., High-protein diet Induces hyperuricemia in a new animal model for studying human gout, Int. J. Mol. Sci. 21 (2020) 2147. https://doi.org/10.3390/ijms21062147.

[22] E. Tapani, M. Taavitsainen, K. Lindros, et al., Toxicity of ethanol in low concentrations. Experimental evaluation in cell culture, Acta Radiol. 37 (1996) 923-926. https://doi.org/10.1177/02841851960373P296.

[23] A.V. Le, T.T. Huynh, S.E. Parks, et al., Bioactive composition, antioxidant activity, and anticancer potential of freeze-dried extracts from defatted gac (*Momordica cochinchinensis* Spreng) Seeds, Medicines 5 (2018) 104. https://doi.org/10.3390/medicines5030104.

[24] M.S. Filigenzi, B. Puschner, L.S. Aston, et al., Diagnostic determination of melamine and related compounds in kidney tissue by liquid chromatography/tandem mass spectrometry, J. Agric. Food Chem. 56 (2008) 7593-7599. https://doi.org/10.1021/jf801008s.

[25] K. Okamoto, B.T. Eger, T. Nishino, et al., Mechanism of inhibition of xanthine oxidoreductase by allopurinol: crystal structure of reduced bovine milk xanthine oxidoreductase bound with oxipurinol, Nucleos. Nucleot. Nucl. 27 (2008) 888-893. https://doi.org/10.1080/15257770802146577.

[26] B. Webb, A. Sali, Protein structure modeling with MODELLER, Methods Mol. Biol. 1654 (2017) 39-54. https://doi.org/10.1007/978-1-4939-7231-9_4.

[27] D. Seeliger, B.L. de Groot, Ligand docking and binding site analysis with PyMOL and Autodock/Vina, J. Comput. Aided Mol. Des. 24 (2010) 417-422. https://doi.org/10.1007/s10822-010-9352-6.

[28] N.M. O'Boyle, M. Banck, C.A. James, et al., Open Babel: an open chemical toolbox, J. Cheminform. 3 (2011) 33. https://doi.org/10.1186/1758-2946-3-33.

[29] J. Eberhardt, D. Santos-Martins, A.F. Tillack, et al., AutoDock Vina 1.2.0: new docking methods, expanded force field, and Python bindings, J. Chem. Inf. Model. 61 (2021) 3891-3898. https://doi.org/10.1021/acs.jcim.1c00203.

[30] G. Schwarz, R.R. Mendel, Molybdenum cofactor biosynthesis and molybdenum enzymes, Annu. Rev. Plant Biol. 57 (2006) 623-647. https://doi.org/10.1146/annurev.arplant.57.032905.105437.

[31] X. Lu, X. Zhao, C. Bai, et al., LC-MS-based metabonomics analysis, J. Chromatogr. B Analyt. Technol. Biomed. Life Sci. 866 (2008) 64-76. https://doi.org/10.1016/j.jchromb.2007.10.022.

[32] H. Luo, Y. Xiang, X. Fang, et al., BatchDTA: implicit batch alignment enhances deep learning-based drug-target affinity estimation, Brief. Bioinform. 23 (2022) bbac260. https://doi.org/10.1093/bib/bbac260.

[33] J. Li, H.A. Chase, Development of adsorptive (non-ionic) macroporous resins and their uses in the purification of pharmacologically-active natural products from plant sources, Nat. Prod. Rep. 27 (2010) 1493-1510. https://doi.org/10.1039/c0np00015a.

[34] M.M. de Freitas, P.R. Fontes, P.M. Souza, et al., Extracts of *Morus nigra* L. leaves standardized in chlorogenic acid, rutin and isoquercitrin: tyrosinase inhibition and cytotoxicity, PLOS ONE 11 (2016) e0163130. https://doi.org/10.1371/journal.pone.0163130.

[35] L. Kolozsvári, A. Nógrádi, B. Hopp, et al., UV absorbance of the human cornea in the 240-to 400-nm range, Invest. ophthalmol. Vis. Sci. 43 (2002) 2165-2168.

[36] S.R. Kalb, J. Lou, C. Garcia-Rodriguez, et al., Extraction and inhibition of enzymatic activity of botulinum neurotoxins/A1, /A2, and /A3 by a panel of monoclonal anti-BoNT/A antibodies, PLOS ONE 4 (2009) e5355. https://doi.org/10.1371/journal.pone.0005355.

[37] D.A. Case, T.E. Cheatham III, T. Darden, et al., The Amber biomolecular simulation programs, J. Comput. Chem. 26 (2005) 1668-1688. https://doi.org/10.1002/jcc.20290.

[38] J.A. Maier, C. Martinez, K. Kasavajhala, et al., ff14SB: improving the accuracy of protein side chain and backbone parameters from ff99SB, J. Chem. Theory. Comput. 11 (2015) 3696-3713. https://doi.org/10.1021/acs.jctc.5b00255.

[39] D. Vassetti, M. Pagliai, P. Procacci, Assessment of GAFF2 and OPLS-AA general force fields in combination with the water models TIP3P, SPCE, and OPC3 for the solvation free energy of druglike organic molecules, J. Chem. Theory Comput. 15 (2019) 1983-1995. https://doi.org/10.1021/acs.jctc.8b01039.

[40] P. Mark, L. Nilsson, Structure and Dynamics of the TIP3P, SPC, and SPC/E water models at 298 K, J. Phys. Chem. 105 (2001) 9954-9960. https://doi.org/10.1021/jp003020w.

[41] R.W. Wilson, V.A. Bloomfield, Counterion-induced condensation of deoxyribonucleic acid. A light-scattering study, Biochemistry 18 (1979) 2192-2196. https://doi.org/10.1021/bi00578a009.

[42] H.C. Andersen, Rattle: a "velocity" version of the shake algorithm for molecular dynamics calculations, J. Comput. Phys. 52 (1983) 24-34. https://doi.org/10.1016/0021-9991(83)90014-1.

[43] Y. Miao, V.A. Feher and J.A. McCammon, Gaussian accelerated molecular dynamics: unconstrained enhanced sampling and free energy calculation, J. Chem. Theory Comput. 11 (2015) 3584-3595. https://doi.org/10.1021/acs.jctc.5b00436.

[44] E. Wang, G. Weng, H. Sun, et al., Assessing the performance of the MM/PBSA and MM/GBSA methods. 10. Impacts of enhanced sampling and variable dielectric model on protein-protein interactions, Phys. Chem. Chem. Phys. 21 (2019) 18958-18969. https://doi.org/10.1039/c9cp04096j.

[45] V.N. Maiorov, G.M. Crippen, Significance of root-mean-square deviation in comparing three-dimensional structures of globular proteins, J. Mol. Biol. 235 (1994) 625-634. https://doi.org/10.1006/jmbi.1994.1017.

[46] M.Y. Lobanov, N.S. Bogatyreva, O.V. Galzitskaya, Radius of gyration as an indicator of protein structure compactness, Mol. Biol. 42 (2008) 623-628. https://doi.org/10.1134/S0026893308040195.

[47] S. Mitternacht, FreeSASA: an open source C library for solvent accessible surface area calculations, F1000Res 5 (2016) 189. https://doi.org/10.12688/f1000research.7931.1.

[48] E. Fuglebakk, J. Echave, N. Reuter, Measuring and comparing structural fluctuation patterns in large protein datasets, Bioinformatics 28 (2012) 2431-2440. https://doi.org/10.1093/bioinformatics/bts445.

[49] D.R. Roe, T.E. Cheatham III, PTRAJ and CPPTRAJ: software for processing and analysis of molecular dynamics trajectory data, J. Chem. Theory Comput. 9 (2013) 3084-3095. https://doi.org/10.1021/ct400341p.

[50] H. Abdi, L.J. Williams, Principal component analysis, Wiley Interdisciplinary Reviews: Computational Statistics 2 (2010) 433-459. https://doi.org/10.1002/wics.101.

[51] D.J. Wales, T.V. Bogdan, Potential energy and free energy landscapes, Phys. Chem. B 110 (2006) 20765-20776. https://doi.org/10.1021/jp0680544.

[52] B.E. Husic, V.S. Pande, Markov state models: from an art to a science, J. Am. Chem. Soc. 140 (2018) 2386-2396. https://doi.org/10.1021/jacs.7b12191.

[53] C. Wehmeyer, M.K. Scherer, T. Hempel, et al., Introduction to Markov state modeling with the PyEMMA software—v0. 3.

[54] G. Perez-Hernandez, F. Noe, Hierarchical time-lagged independent component analysis: computing slow modes and reaction coordinates for large molecular systems, J. Chem. Theory Comput. 12 (2016) 6118-6129. https://doi.org/10.1021/acs.jctc.6b00738.

[55] R. Metzler, J. Klafter, From a generalized Chapman Kolmogorov equation to the fractional Klein Kramers equation, Phys. Chem. B 104 (2000) 3851-3857. https://doi.org/10.1021/jp9934329.

[56] P. Deuflhard, M. Weber, Robust Perron cluster analysis in conformation dynamics, Linear Algebra Appli. 398 (2005) 161-184. https://doi.org/10.1016/j.laa.2004.10.026.

[57] E. Vanden-Eijnden, Transition path theory, in: M. Ferrario, G. Ciccotti, K. Binder (Eds.), Computer simulations in condensed matter systems: from materials to chemical biology volume 1, Springer, 2006, pp. 453-493,

[58] V.F. Azevedo, I.A. Kos, A.B. Vargas-Santos, et al., Benzbromarone in the treatment of gout, Adv. Rheumatol. 59 (2019) 37. https://doi.org/10.1186/s42358-019-0080-x.

[59] A. Davenport, M.F. Sheikh, E. Lamb, et al., Acute kidney injury in acute-on-chronic liver failure: where does hepatorenal syndrome fit? Kidney Int. 92 (2017) 1058-1070. https://doi.org/https://doi.org/10.1016/j.kint.2017.04.048.